Defect and magnetic structure of Y2.93La0.07Fe5O12/Gd3Ga5O12 epitaxial systems

Fodchuk, Ihor, Hutsuliak, Ivan, Dovganyuk, Volodymyr, Sumariuk, Oleksandr, Gudymenko, Oleksandr, et al.

Ihor Fodchuk, Ivan Hutsuliak, Volodymyr Dovganyuk, Oleksandr Sumariuk, Oleksandr Gudymenko, Vasyl Kladko, Ivan Syvorotka, Andrii Kotsyubynskiy, Michael Barchuk, "Defect and magnetic structure of Y2.93La0.07Fe5O12/ Gd3Ga5O12 epitaxial systems," Proc. SPIE 11369, Fourteenth International Conference on Correlation Optics, 113691G (6 February 2020); doi: 10.1117/12.2553969

SPIE.

Event: Fourteenth International Conference on Correlation Optics, 2019, Chernivtsi, Ukraine

Defect and magnetic structure of $Y_{2.93}La_{0.07}Fe_5O_{12}/Gd_3Ga_5O_{12}$ epitaxial systems

Ihor Fodchuk,[a,*] Ivan Hutsuliak,[a] Volodymyr Dovganyuk,[a] Oleksandr Sumariuk,[a] Oleksandr Gudymenko,[b] Vasyl Kladko,[b] Ivan Syvorotka,[c] Andrii Kotsyubynskiy,[a] Michael Barchuk,[d]

[a]Chernivtsi National University, Kotsjubynskyi str. 2, Chernivtsi, Ukraine
[b]Institute of Semiconductor Physics of NASU, Nauky str. 41, Kyiv, Ukraine
[c] Institute for Applied Problems of Mechanics and Mathematics of NASU, Naukova str. 3-b, Lviv, Ukraine
[d] Institute of Materials Science, TU Bergakademie Freiberg, Gustav-Zeuner-Str. 5, Freiberg, Germany

Abstract. This work presents the results of investigation of crystal structure of yttrium iron garnet films of different thickness using high-resolution X-ray diffractometry data and simulation of X-ray intensity distributions in the vicinity of the reciprocal lattice points by the Monte Carlo approach. The parameters of films column microstructure are determined and substantiated, and the model of their defective structure as systems of two types of dislocations with different directions of the Burgers vector is proposed.

Keywords: yttrium iron garnet, epitaxial film, X-ray diffractometry, magnetic domain structure, Monte Carlo method.

***Ihor Fodchuk, E-mail: ifodchuk@ukr.net

1 Introduction

For many years, epitaxial films with the garnet structure have been finding a wide application in modern microwave engineering and microelectronics, in particular, in sensor devices for visualization of magnetic field, super high-frequency bandpass filters, solid-state lasers, non-volatile magnetic memory systems[1-3]. Recent developments are focused on the use of garnet films known as yttrium iron garnets (YIG) in the new generation of spin nanoelectronic devices working at microwave frequency[4,5]. The manufacture of magneto-optical or microwave devices requires iron garnets with predesigned technical parameters. Therefore, microstructural investigation of such epitaxial films is of highest importance. Nowadays, many works are dedicated to the study of structural, magneto-optical, temperature and other properties of garnet films[6-12]. For example, the dependence of magnetic characteristics of garnet films on their structural imperfections has been observed in work[8]. It has been shown that the garnet epitaxial films are structurally perfect enough, although they contain microstresses caused by presence of the transition layer, which appears because of the lattice mismatch between the grown film and the substrate[9]. O'Dell has revealed that garnet films commonly inherit defects, which already exist on the surface of the used substrates[10].

The investigation of the structural parameters enables to understand their impact on the formation of the domain structure of iron garnets and, therefore, to control and possibly modify the growth process. Recently, we have studied the influence of N^+ ion implantation on the microstructural and magnetic properties of the La-doped yttrium iron garnet (YIG) films. In this paper, we report on investigation of a set of YLaFeO epitaxial films using the combination of the high-resolution X-ray diffraction (HRXRD) and the Monte Carlo simulation of reciprocal space maps (RSMs) to investigate the influence of the thickness of YIG films under study and their structural perfection on magnetic properties.

Fourteenth International Conference on Correlation Optics, edited by Oleg V. Angelsky, Proc. of SPIE Vol. 11369, 113691G · © 2020 SPIE
CCC code: 0277-786X/20/$21 · doi: 10.1117/12.2553969

2 Object and methods of research

In this contribution, we investigated [111]-oriented iron garnet epitaxial films commercially grown by Scientific Research Company "Carat" at "Garnet 3" facility with five heating zones. As substrates, gadolinium gallium garnet $Gd_3Ga_5O_{12}$ (GGG) with (111) surface orientation were used. The deposition process of epitaxial YIG films of nominal composition $Y_{2.93}La_{0.07}Fe_5O_{12}$ was performed by isothermal liquid-phase epitaxy from overcooled melt solution based on PbO-B_2O_3 components[13,14]. All technological investigations were performed on air. The growth temperature was in range 940.. 960 °C (Table 1). The thicknesses of grown films were determined by weighing them taking into account calculated film density. A set of films with thicknesses 6.4 μm (S1), 55.1 μm (S2), 70.7 μm (S3) and 94.4 μm (S4) were selected for the study.

Table 1 Growth parameters of $Y_{2.93}La_{0.07}Fe_5O_{12}$ epitaxial films. $R_1=Fe_2O_3/Y_2O_3$, $R_3=PbO/B_2O_3$, R_4=garnet/(garnet+solution), $K_1=Y_2O_3/La_2O_3$ are the mass ratios of solution components

Sample	Thickness, μm	Growth speed, μm/min.	Substrate temperature, °C	R_1	R_3	R_4	K_1
S1	6.41	0.642	945	30.8	12	13.6	12.9
S2	55.16	0.424	953-944	31	12	13.6	12.7
S3	70.71	0.589	960	30	15.6	13.8	10
S4	94.4	0.59	950	29.5	12	13.6	13.3

The microstructural studies of YIG films were carried out at a high-resolution X-ray diffractometer X'Pert PRO MRD equipped with a triple-axis setup. In order to perform a high-resolution reciprocal space mapping, we utilized Göbel parabolic mirror placed behind the X-ray tube producing Cu $K_{\alpha 1}$ radiation. The mirror was followed by four-crystal Bartels monochromator (4×Ge220), 3-bounce analyzer crystal (3×Ge220), and point detector. The divergence of the primary beam and the angular acceptance of the analyzing crystal used in front of the detector were estimated as $\Delta\alpha_i=\Delta\alpha_f\approx$12 arcsec.

3 Investigation of ferromagnetic properties

Many parameters of YIG films, such as saturation magnetization, ferromagnetic resonance (FMR) linewidth $2\Delta H$ and anisotropy field depend on the distribution of cations between sublattices, the presence of oxygen vacancies, divalent iron ions and mechanical stresses[6,7]. Iron garnets possess cubic symmetry and belongs to the space group O_h^{10} – $Ia3d$. The iron ions Fe^{3+} occupy octahedral and tetrahedral sites in the ratio 2:3 and form two magnetic sublattices with oppositely directed spins, which predefines magnetic behavior of this material. Even with the 100 % reproduction of the technological conditions of growth, such as a growth temperature, a degree of supercooling of the melt solution, a speed of rotation of the substrate, etc., there still will be slight change in physical properties between films due to depletion of the melt[8].

The FMR linewidth determines electromagnetic losses of a microwave device, and the smaller $2\Delta H$ parameter are, the smaller losses will be[6,7,9]. The quality of YIG film is decreased by presence of defects, impurity ions and oxygen vacancies in crystalline structure, heterogeneity of thickness and

lateral chemical composition. All these factors lead to a broadening of the FMR linewidth and an increase in electromagnetic losses[10].

The FMR linewidth measurement was performed by a non-destructive FMR spectrometer at a frequency of 3 GHz, based on local excitation of a magnetic wave resonance at a small area of the film surface by a magnetic displacement field with a hole-shaped profile[13] (Fig. 1).

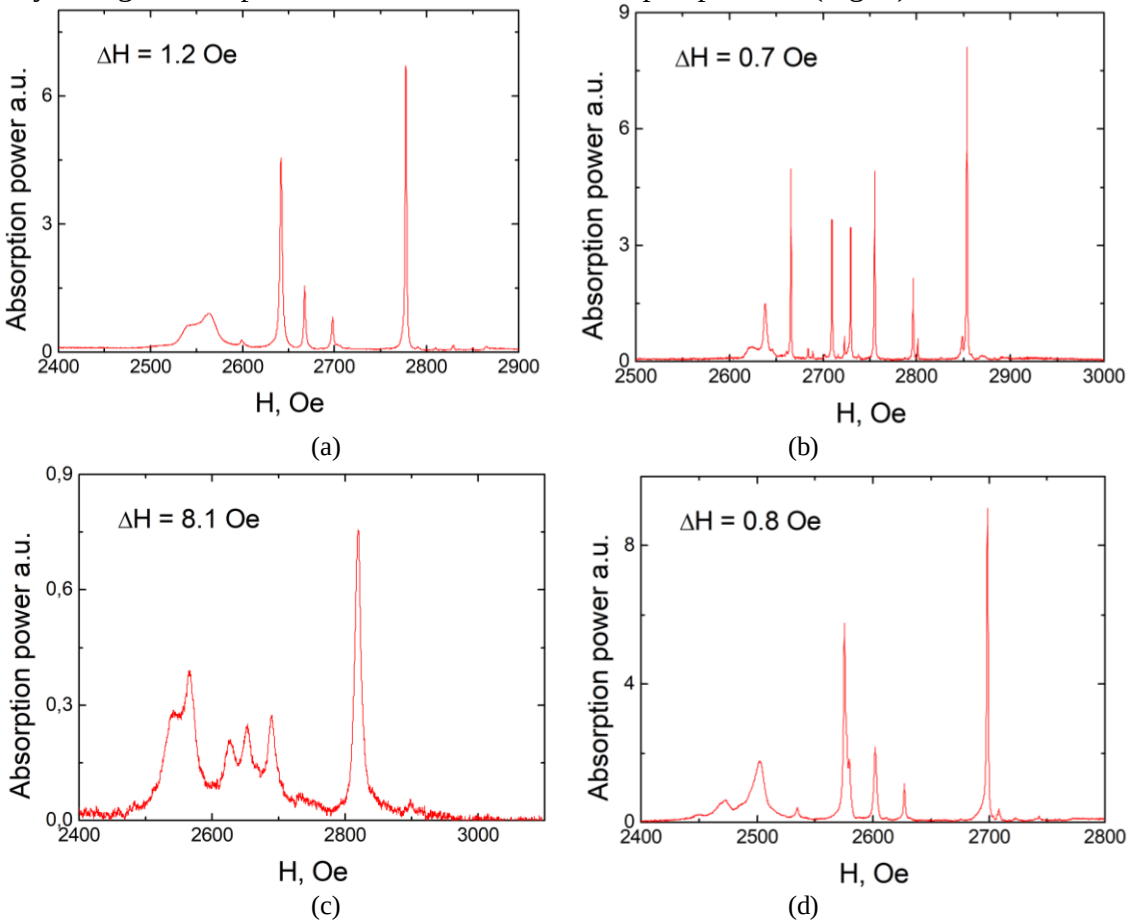

Fig. 1 FMR spectra at 3 GHz for YIG samples S1 (a), S2 (b), S3 (c) and S4 (d).

Conditions of the ferromagnetic resonance were provided using a hole-shaped profile of a constant magnetic field created by a hole in one of electromagnet poles; YIG sample under study was placed inside of the gap of magnet. A significant advantage of this method is the ability to locally measure the FMR linewidth in full-size epitaxial structures (up to 3 inches (76.2 mm) in diameter) without destroying them. The FMR linewidth is highly dependent on the surface morphology and is an order of magnitude smaller for films with a smooth surface than for films whose surface has a significant roughness[13,15] (tens of nm). In turn, the structural perfection of the surface depends primarily on the growth conditions and the defective structure of sample itself.

4 Theoretical relations

Different approaches of kinematic Krivoglaz theory[16] and dynamic diffraction theories[17-19] can be used to simulate RSMs.

If one limits himself to the case of distortions, when atomic planes are displaced relatively to the positions in ideal crystal without changing their scattering ability, then the polarization of the real crystal $\chi(\mathbf{r})$ can be decomposed into a Fourier series[20,21]

$$\chi(\vec{r}) = \sum_g \chi_g(\vec{r}) e^{i\vec{g}(\vec{r}-\delta\vec{u}(r))} = \sum_{\mathbf{g}} \chi_{\mathbf{g}}(\vec{r}) e^{i\vec{g}_{def}(\vec{r}-\delta\vec{u}(r))}, \quad (1)$$

where $\vec{g}$ is the reciprocal lattice vector, $\chi_g(\vec{g})$ is the gth component of Fourier polarization, $\vec{u}(r)$ is the field of random displacements in crystal, in particular:

$$\vec{u}(r) = \langle\vec{u}(r)\rangle + \delta\vec{u}(r), \vec{g}_{def} = \vec{g} - \nabla(\vec{g}\cdot\langle\vec{u}(r)\rangle). \quad (2)$$

Here $\vec{g}_{def}$ is a vector of averaged reciprocal lattice. In following we'll drop lower index "def".

In the presence of a high concentration of dislocations in crystals, a complete differential scattering cross section (coherent + diffuse components) will be[22]

$$\frac{d\sigma}{d\Omega} = \frac{K^4}{16\pi^4}\left|\chi_g\right|^2 \iiint d^3\vec{r} \iiint d^3\vec{r}' G_g(\vec{r},\vec{r}') e^{-ig(\vec{r}-\vec{r}')} \quad (3)$$

where V is the volume of the sample, Ω is the form function and the Green Function G_g is

$$G_g(\vec{r},\vec{r}') = \langle e^{-ig(\vec{u}(\vec{r})-\vec{u}(\vec{r}'))}\rangle \equiv e^{-T_g(\vec{r},\vec{r}')}, \text{ a } \vec{u}(\vec{r}_n) \equiv \vec{u}_n = \sum_\alpha \sum_m c_m^\alpha \vec{v}_{nm}^\alpha. \quad (4)$$

Here $\vec{c}^\alpha$ is the concentration of α-type dislocations, $\vec{v}^\alpha$ is the displacement field from α-type dislocations, T is scattering operator, which in the kinematic approximation is $T \approx V$, where V is the scattering potential.

In the kinematic approximation of the scattering theory, amplitude of coherent part of scattered wave is proportional to

$$\langle E\rangle \infty \iiint d^3\vec{r}\langle\chi_g(\vec{r}) e^{-ig\delta\vec{u}(\vec{r})}\rangle e^{-ig\vec{r}}. \quad (5)$$

If sample is statistically homogeneous, then

$$\langle\chi_g(\vec{r}) e^{-ig\delta\vec{u}(\mathbf{r})}\rangle = \chi_g e^{-D}, \quad (6)$$

where $0 < e^{-D} < 1$ is static Debye-Waller factor.

Usually, dislocations positions in real crystals are highly correlated[23]. In this case, the expression for T will be

$$T_h(\vec{r}_n,\vec{r}_m) \equiv T_{\mathbf{h}nm} = T_{\mathbf{h}nm}^{(1)} + T_{\mathbf{h}nm}^{(2)}, \quad (7)$$

where

$$T_{hnm}^{(1)} \approx \sum_{\alpha,k} c^\alpha \Phi_{nmk}^\alpha \; ; \; \Phi_{nmk}^\alpha = 1 - e^{-i\vec{h}(\vec{v}_{nk}^\alpha - \vec{v}_{mk}^\alpha)} \; ; \rho^\alpha = c^\alpha/a^n \quad (8)$$

is uncorrelated addition, and

$$T_{hnm}^{(2)} \approx -\frac{1}{2}\sum_{(\alpha,k)\neq(\beta,\delta)}\langle\delta c_k^\alpha \delta c_s^\beta\rangle \Phi_{nmk}^\alpha \Phi_{nms}^\beta \; , \delta c_k^\alpha = c_k^\alpha - c^\alpha \quad (9)$$

includes two-point correlation, described by correlation function

$$\varepsilon_{ks}^{\alpha\beta} = \langle\delta c_k^\alpha \delta c_s^\beta\rangle, \quad (10)$$

where n is a dimension of dislocation array, ρ^α is n-dimensional dislocation density, and it is also assumed that $c^\alpha << 1$.

Within this theory, using the Monte Carlo method, based on relations (7)–(10), one can calculate the intensity of scattered radiation $I(Q_x, Q_z)$ in the case of a possible dislocation system in YIG films[24].

5 High-resolution X-ray diffraction

The YIG films grown on (111)-oriented GGG substrate have a rhombohedral structure[25]. The lattice parameter of the substrate is a_{GGG}=12,383 Å, and for the film a_{YIG}=12,376 Å[26]. The non-zero difference of lattices parameter of film and substrate during growth leads to a presence of deformations

inside of the film, which repeats translation structure of the substrate in the plane of growth. This is also accompanied by the appearance of a large number of mismatch dislocations.

The analysis of the experimental distributions of intensity $I_h(q_x,q_z)$ around the reciprocal space points (Figs. 2, 3) was performed using the Krivoglaz kinematic theory[16,27], which well describes the diffuse scattering of X-waves in crystals containing high dislocation densities. As the column structure is typical for the garnet layers[28,29], the systems of edge and screw dislocations with the dislocation lines normal to the surface can be selected as a model of the dominant defects in the epitaxial film and the transition layer[30].

The basic glide planes in garnet are {110} and {112} planes with <111>, <110>, and <113> glide directions[29,30]. For our model, $\{11\bar{2}\}$ planes were selected as the glide planes, so the lines of edge and screw dislocations were oriented perpendicular to the sample surface (in [111] direction). The Burgers vectors of the mentioned dislocations were chosen as $\vec{b}_s = a[111]/2$ for the system of screw dislocations and $\vec{b}_e = a[\bar{1}10]$ for the system of edge ones. In other words, we considered a model of a stacking sequence inside the individual columns, which are surrounded by uniformly distributed dislocations[30,31]. This approach enabled using of the Monte Carlo method, which includes the surface stresses relaxation for the RSMs calculation. To calculate the penetration depth Λ_B, we employed well-known formulae and theoretical data of Fourier polarizability coefficients of a defect-free iron garnet crystal together with atomic form factors and absorption cross-sections[32,33].

The reciprocal space maps calculated for all samples using the Monte Carlo model are represented in Fig. 2 and 3 (b, d and f plots). The simulated intensity distributions are found to be in a satisfying agreement with experimental data. The densities of uniformly distributed screw and edge dislocations obtained as input parameters from the Monte Carlo simulation as well as the lateral column sizes from the Williamson-Hall plot are listed in Table 2. From the simulation, it follows that the edge dislocations predominantly provide a major contribution to the broadening of the reciprocal lattice points.

Table 2 Average lateral column sizes and densities of screw $\vec{b}_s = a[111]/2$ and edge $\vec{b}_e = a[\bar{1}10]$ dislocations

Sample	Column size, μm	Dislocation density, cm^{-2}	
		Edge	Screw
S1 (6.4 μm)	2.25	$3{,}26 \cdot 10^7$	$3{,}92 \cdot 10^5$
S2 (55.1 μm)	2.48	$5.3 \cdot 10^6$	$1.9 \cdot 10^5$
S3 (70.7 μm)	3.725	$3.59 \cdot 10^5$	$2.1 \cdot 10^5$
S4 (94.4 μm)	2.6	$3{,}26 \cdot 10^7$	$3{,}92 \cdot 10^5$

The use of more complicated models of defect systems within the kinematic theory of diffraction[16,21,27,34] or the application of the dynamical theory of diffraction based on the solution of the system of Takagi equations[19] may provide RSMs more similar to experimental $I_h(q_x, q_z)$ distributions.

Sample S1, despite its relatively small thickness has a well-formed crystalline structure, as evidenced by typical symmetric $I_h(q_x, q_z)$ distribution on RSM (Fig. 2a). The additional intensity maximum shifted along the q_z axis by 0.001 $Å^{-1}$ from the well-pronounced YIG peak comes from the interface transitional film-substrate layer, since the angular distance between the peaks does not correspond to the position of the substrate reciprocal point. In addition, the extinction depth for (444)

reflection $\Lambda_B^{444} = 2.25$ μm is less than the thickness of the film (t=6,41 μm). The sample has a considerable density of dislocations and a well-defined mosaicity of the crystalline structure, as evidenced by broadening of the intensity distribution along q_x axis in RSM, and confirmed by the simulation results (Fig. 2b, Table 1). However, FMR linewidth value is not significant, which is probably due to the relaxation of crystal lattice of the film and its surface during the growing process. $I_h(q_x, q_z)$ distribution is asymmetric along q_x axis, this may indicate insignificant densities of the vacancy-type inclusions, possibly with oxygen complexes in {100} planes[29].

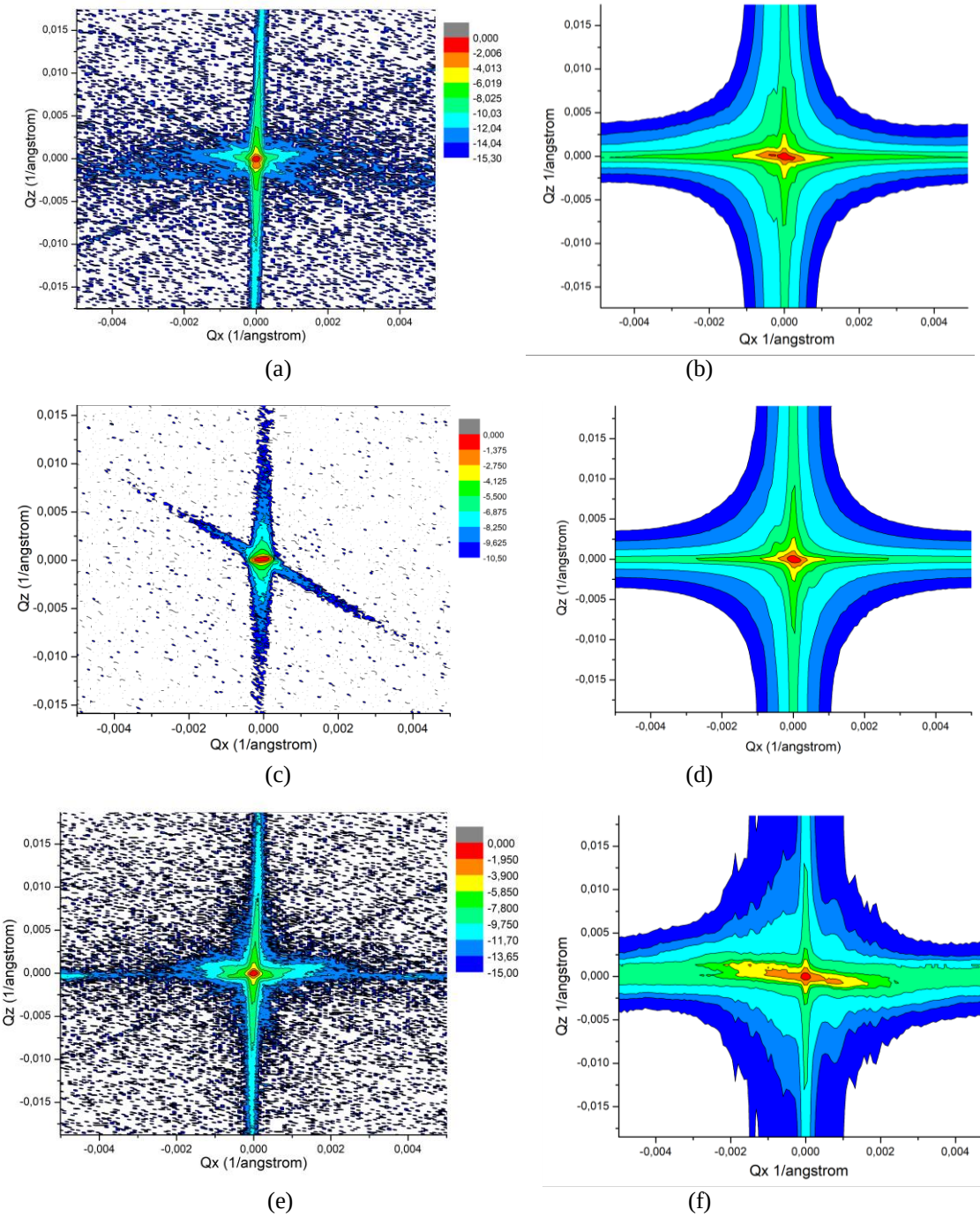

Fig. 2 $I_h(q_x, q_z)$, S1 (a, b), S2 (c, d), S4 (d, e), (444), Cu $K_{\alpha 1}$, $\Lambda_B^{444} = 2.25$ μm: a), c), e) – experiment; b), d), f) – simulation.

The RSM of sample S2 practically has no broadening around the peak along q_x axis – lateral stresses in the film are minimal. The crystal structure is well formed, and the film has homogeneous distribution of microdefects, which is also confirmed by simulation –sample S2 has very low density of defects. There is a distinct strike from the analyzer crystal, unlike other films, which is due to a smooth, practically mirror, homogeneous surface of the film with low surface roughness[13,14] (~ 10 nm). Such surface structure provides the best magnetic properties of the material[13,14].

The RSM of sample S3 (t=70.71 μm) shown in Fig. 3a is slightly different in comparison to the previous samples. Strong diffuse scattering at smaller q_z values and asymmetrical intensity distribution along the q_x axis indicate the gradient of residual deformations in the near-surface region and high dislocation density (Table 1). In particular, there can be significant densities of dislocation loops of small sizes, which are a specific feature of growth conditions[29].

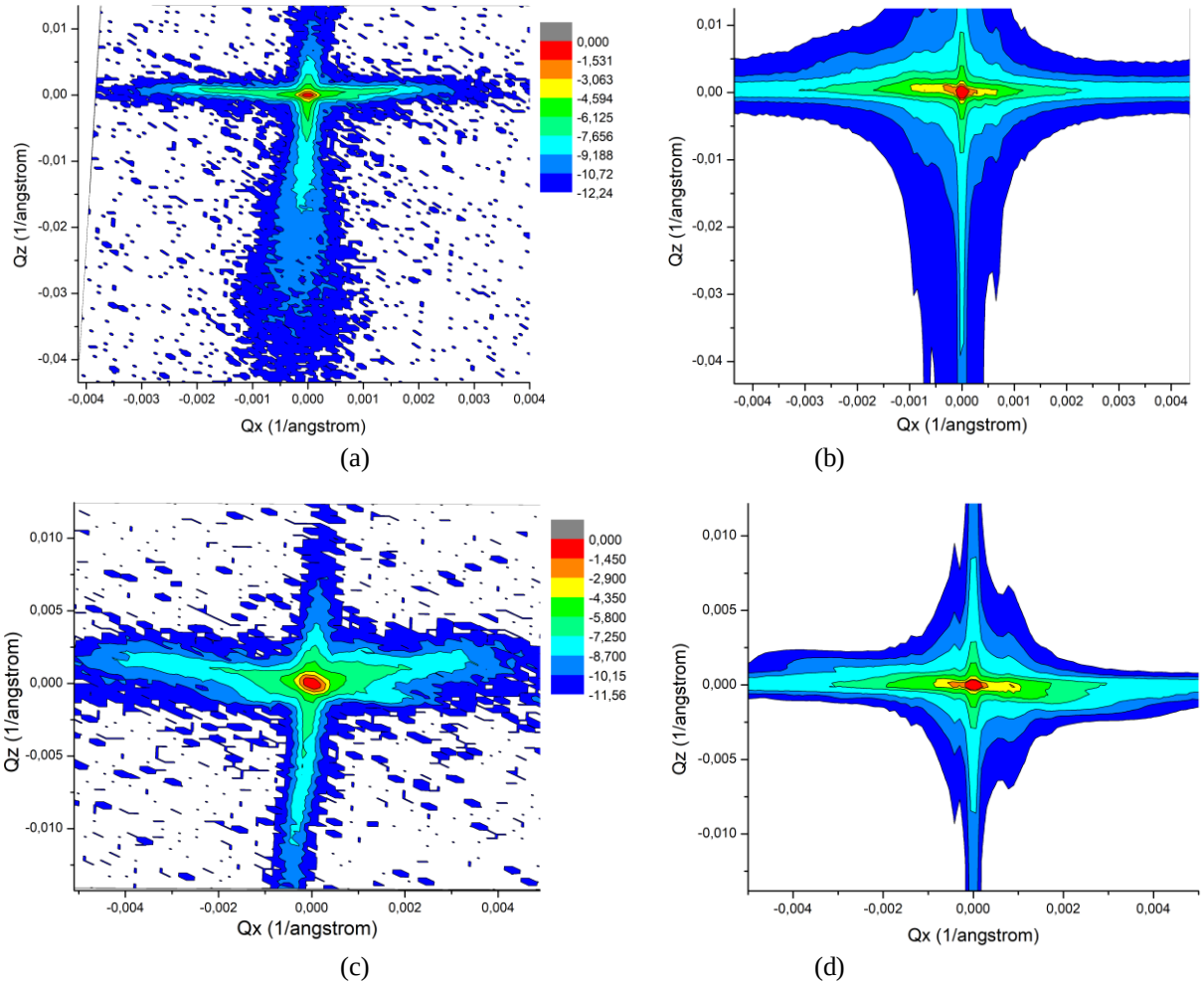

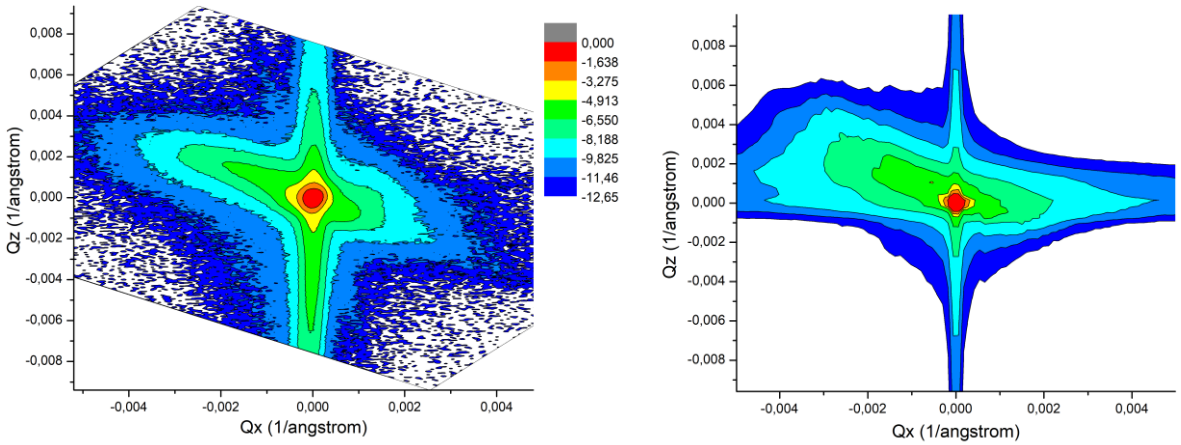

(e) (f)

Fig. 3 $I_h(q_x, q_z)$, S3, t=70.71 μm, Cu $K_{\alpha 1}$. Experiment: a) (444), $\Lambda_B^{444} = 2.25$ μm, c) (888), $\Lambda_B^{888} = 12.82$ μm, e) (880) $\Lambda_B^{880} = 13.24$ μm. Simulation: b) (444), d) (888), f) (880).

The presence of residual stresses at the surface layer can be estimated from the positions of maxima in experimental 444, 888 and 880 RSMs, according to which sample S3 possesses compressive residual strain of $\varepsilon=(a_0-a)/a_0=-3.1\cdot10^{-4}$ that indicates the partial relaxation of the layer. It can be caused either by deviation stoichiometric composition of components distribution during growth or by the presence of microdefects, for example, complexes with oxygen[29,35], which, in turn, caused the appearance of a specific blur for (444) reflection (Figs. 3a).

In Fig. 3c and 3e for symmetrical 888 and asymmetrical 880 RSMs reflections, one can see more uniform distribution of defects with increase of the film thickness, so the effect of the transition film/substrate layer disappears. Since Λ_B^{444} is almost 6 times lower than Λ_B^{888}, it can be argued that this film is structurally homogeneous in the volume. However, it still has some residual stresses in the near-surface layer of relatively small thickness. At the same time, the bend of intensity distribution along q_x axis in Fig. 5c confirms the presence of the packing defects, possibly oxygen complexes in the planes of close packing[34]. This is partly confirmed by the results of simulation – dislocation densities and column sizes (Table 2). In fact, there is an intermediate state between a well-formed structure and a film surface, with a noticeable effect of the surface and the transition layer on a bulk crystal structure. The film possesses the lowest dislocation density according to structure simulation data, which may be due to the presence of long boundaries between columns with larger diameter and a higher growth temperature, which influences formation of the transition layer.

The symmetrical 444 RSM shown in Fig. 2e indicates that sample S4 has well-formed crystalline structure. The presence of an asymmetrical distribution of diffuse scattering for positive Δq_x values, which intensity constantly decays with the increase of Δq_x, testifies the presence of defects that cause tensile deformations[36]. It results in a tensile strain along q_z axis $\varepsilon=-8\cdot10^{-5}$ (the lattice parameter increase up to 12.379 Å). In particular, this effect can occur from extended microdefects with the foreign phase inclusions, microinclusions of the crucible material and oxides of the garnet-forming components[29]. Weak satellite peaks shifted from the main peak along Δq_x axis by -0.005Å^{-1} and 0.004Å^{-1} stem probably from the tilted blocks of the columnar La:YIG structure with an angular misorientation of about 0.08 degrees[12]. The FMR linewidth of sample S4, as for sample S3, is small, notwithstanding the fact that S4 has an order of magnitude greater dislocation density. However, stresses between columns, caused by dislocations, are compensated due to the film thickness. In fact, such structure is

well relaxed, providing homogeneous magnetic properties. But, from a technical point of view, a significant overrun of material compared to S2 is negative for sample S4.

The studied garnet films have mosaic structure, which explains the presence of dislocations surrounding the individual columns and is confirmed by good agreement between simulated and experimental RSMs[8]. The column structure of the iron garnet films with almost constant lateral sizes (~2 μm) was revealed using HRXRD for samples S1, S2, and S4 with different thicknesses. Two times larger lateral size of the columns obtained for sample S3 can be probably explained by the layer deposition at higher temperature. A decrease in the dislocation density is observed with increasing film thickness, which is an evidence of a decrease in the influence of the crystal substrate and the transition layer and, consequently, a decrease in the stresses of the crystalline structure inherent for YIG.

5 Conclusions

1.The crystalline structure of the set of $Y_{2.93}La_{0.07}Fe_5O_{12}$ epitaxial films with different thicknesses and different values of the FMR linewidth was investigated. A model of a defective YIG system with a mosaic structure is proposed, and approximate lateral dimensions of the columns are determined. It is established that their formation depends on the conditions of growth process, in particular on temperature of deposition. Lateral size of the columns increase with increasing growth temperature, and the dislocations density predominantly decreases.

2. It is shown that the films structure depends largely on the influence of the transition layer. It becomes less noticeable with increasing film thickness, which leads to relaxation of internal stresses. Sample S3 due to the increased growth temperature possesses significant lateral stresses, this is especially evident from the data of (880) RSM. As a consequence, this sample has ten times bigger value of the FMR linewidth.

3. The smallest FMR linewidth values are typical for films with low dislocation density and relaxed structure, in particular near-surface layers. The surface of such films has a slight roughness, and for the sample S2 it is ~ 10 nm. The condition of the surface and subsurface layers of the film has a great influence on the formation of the magnetic structure.

4. The defect garnet structure was described as the system of two sets of edge and screw dislocations in $\{11\bar{2}\}$ glide planes with the dislocation lines perpendicular to the surface and the Burgers vectors $\vec{b}_e = a[\bar{1}10]$ and $\vec{b}_s = a[111]/2$. The simulation of the RSMs was performed within the kinematical theory of X-ray diffraction using the Monte Carlo approach in order to determine the density of dislocations. The simulated RSMs showed a good agreement with experimental data. The main contribution to formation of the diffraction pattern was found to stem from the edge dislocations. The increase of the film thickness was accompanied by a decrease of dislocation density and a relaxation of the films, which is the evidence of a decrease in the influence of the crystal substrate and the transition layer and, consequently, a decrease in the stresses of the crystal structure.

References

1. S.B. Ubizskii, “Orientation states of magnetisation in epitaxial (111)-oriented iron garnet films,” *Journal of Magnetism and Magnetic Materials*. **195**(3), 575-582 (1999).

[doi:/10.1016/S0304-8853(99)00165-1]

2. U.L. Rohde, and A.K. Poddar, "Cost-Effective, Power-Efficient and Configurable YIG Replacement Signal Source," *German Microwave Conference-GeMiC*., Germany, 28-30 March, (2006).
3. J. Helszajn, *YIG Resonators and Filters*, John Wiley & Sons, New York (1985).
4. Y. Kajiwara et al, "Transmission of electrical signals by spin-wave interconversion in a magnetic insulator," *Nature*. **464**, 262-266 (2010). [doi:/10.1038/nature08876]
5. K. Uchida et al., "Spin Seebeck insulator," *Nature Materials*. **9**, 894-897 (2010). [doi:/10.1038/nmat2856]
6. G.S. Krinchik et al., "Fine structure of Fe^{3+} absorption lines in single-sublattice garnet ferrites," *Semiconductors/Physics of the Solid State*. **23**(2), 405-412 (1981).
7. S.H. Wemple et al., "Optical properties of epitaxial iron garnet thin films," *Phys. Rev. B.* **9**(5), 2134-2144 (1974). [doi:/10.1103/PhysRevB.9.2134]
8. S.B. Ubizskii, "Orientational states of magnetization in (111)-oriented iron garnet films," *J. Magn. & Magn. Mat*. **195**, 575–582 (1999). [doi:/10.1016/S0304-8853(99)00165-1]
9. V.V. Nemoshkalenko et al., "The degree of structural and magnetic disorder in ferrite-garnet films implanted with boron ions," *Semiconductors/Physics of the Solid State*. **32**(3), 707-713 (1990).
10. T H O Dell, "Magnetic bubble domain devices," *Rep. Prog. Phys*. **49**(5), 589 (1986). [doi:/10.1088/0034-4885/49/5/002]
11. R.C. Linares, E.L. Sloan III., "Epitaxial growth of narrow linewidth yttrium iron garnet films," *Journal of Crystal Growth*. **27**, 249-252 (1974). [doi:/10.1016/S0022-0248(74)80070-9]
12. I.M. Fodchuk et al., "Magnetic force microscopy of YLaFeO films implanted by high dose of nitrogen ions" *Semiconductor Physics, Quantum Electronics & Optoelectronics*. **16**(3), 246-252 (2013). [doi:/10.15407/spqeo16.03]
13. I.I. Syvorotka, I.M. Syvorotka and S.B. Ubizskii, "Thick Epitaxial YIG Films with Narrow FMR Linewidth" *Solid State Phenomena*. **200**, 250-255 (2013). [doi:/10.4028/www.scientific.net/SSP.200.250]
14. I. I. Syvorotka, I. M. Syvorotka, and I. V. Kityk, "Surface morphological changes and magnetic properties of Sc-substituted Y3Fe5O12 epitaxial films deposited on the GGG substrate," *J. Magn. Magn. Mater*. **322**(21), 3314–3319 (2010). [doi:/10.1016/j.jmmm.2010.06.015]
15. I. M. Fodchuk et al., "Magnetic and structural changes in the near-surface epitaxial Y_295La_005Fe_5O_12 films after high-dose ion implantation," *Applied Optics*. **55**(12), B144 (2016). [doi:/ 10.1364/AO.55.00B144]
16. M. A. Krivoglaz, *X-Ray and Neutron Diffraction in Nonideal Crystals*, Springer, Berlin (1996).
17. A. Authier, *Dynamical Theory of X-Ray Diffraction*, Oxford University Press (2001).
18. L. I. Datsenko, V. B. Molodkin, M. E. Osinovsky, *Dynamic scattering of X-rays by real crystals*, Naukova Dumka, Kiev (1988).
19. S. Takagi, "A Dynamical Theory of Diffraction for a Distorted Crystal," *J. Phys. Soc. Jpn*. **26**(5), 1239 (1969). [doi:/10.1143/JPSJ.26.1239]
20. V. B. Molodkin et al., "Dynamical Theory of Triple-Crystal X-Ray Diffractometry and Characterization of Microdefects," *Metallofiz. Noveishie Tekhnol.* **38**(1)99-139 (2016). [doi:10.15407/mfint.38.01.0099]
21. Y. I. Nesterets and V. I. Punegov, "The statistical kinematical theory of X-ray diffraction as applied to reciprocal-space mapping," *Acta Cryst A*. **56**(6), 540-548 (2000). [doi:/10.1107/S010876730000996X]

22. Z. Swiatek, and I. M. Fodchuk, "X-ray topography of the subsurface single-crystal layers in a skew asymmetric pattern of diffraction in the reflection geometry," *Archives of Metallurgy and Materials*. **61**(4), 1931-1938 (2016). [doi:10.1515/amm-2016-0310]
23. Z. Swiatek, I. Fodchuk, and R. Zaplitnyy, "Direct and Inverse Problems in X-ray Three-crystal Triple Laue case X-ray topography of subsurface crystal layers," *Journal of Applied Crystallography*. **50**(3), 727-733 (2017). [doi:/10.1107/S1600576717007208]
24. V. M. Kaganer, and K. K. Sabelfeld, "X-ray diffraction peaks from partially ordered misfit dislocations," *Physical Review B*. **80**(18), 184105 (2009). [doi:/10.1103/PhysRevB.80.184105]
25. O.G. Rutkin et al., "Deformation of the crystal lattice of epitaxial films of yttrium iron garnet grown on the (111) plane of a gadolinium-gallium garnet substrate," *Technical Physics Letters.* **52**(12), 82-86 (1982).
26. H. Levinstein et al., "Growth of High-Quality Garnet Thin Films from Supercooled Melts," *Appl. Phys. Lett*. **19**(11), 486 (1971). [doi:/10.1063/1.1653784]
27. V. Holy, U. Pietsch, and T. Baumbach, *High-resolution X-ray scattering from thin films and multilayers*, Springer, Berlin (1999).
28. A.P. Tankeev, M.A. Borich, and V.V. Smagin, "Dynamics of a spiral magnetic structure in an external magnetic field," *The Physics of Metals and Metallography* **115**(5), 425-436 (2014). [doi:/10.1134/S0031]
29. A. A. Blistanov, "Crystals for Quantum and Nonlinear Optics," *2nd Edition, MISIS Publisher*, Moscow (2007).
30. M. Barchuk et al., "X-ray diffuse scattering from threading dislocations in epitaxial GaN layers," *J. Appl. Phys.* **108**, 043521 (2010). [doi.org/10.1063/1.3460803]
31. S. Daniš et al., "High-resolution diffuse x-ray scattering from threading dislocations in heteroepitaxial layers," *Appl. Phys. Lett*. **85**(15), 3065-3067 (2004). [doi.org/10.1063/1.1806279]
32. D. Waasmaier and A. Kirfel, "New analytical scattering-factor functions for free atoms and ions," *Acta Crystallogr. A*. **51**(3), 416-431 (1995). [doi.org/10.1107/S0108767394013292]
33. R. W. James, "The Dynamical Theory of X-Ray Diffraction," *Solid State Phys*. **15**: 53 (1963). [doi:/10.1016/S0081-1947(08)60592-5]
34. V.B. Molodkin et al., "X-ray diffraction characterization of microdefects in silicon crystals after high-energy electron irradiation," *Phys. Stat. Sol. A.* **208**(11), 2552–2557 (2011). [doi:/10.1002/pssa.201184253]
35. V.M. Pilipiv et al., "Dynamical diffractometry of structural defects and deformation in garnet plating systems $Y_3Fe_5O_{12}/Gd_3Ga_5O_{12}$," *Metallofiz. Noveishie Tekhnol.* **33**(9), 1147-1174 (2011). [doi.org/10.15407/mfint]
36. V.T. Bagel et al., "Study of the features of the formation of microdefects in heat-treated dislocation-free silicon wafers of large diameter by diffuse x-ray scattering," *Semiconductors/Physics of the Solid State.* **45**(10), 1825-1832 (2003).

Caption List

Fig. 1 FMR spectra at 3 GHz for YIG samples S1 (a), S2 (b), S3 (c) and S4 (d).
Fig. 2 $I_h(q_x, q_z)$, S1 (a, b), S2 (c, d), S4 (d, e), (444), Cu $K_{\alpha 1}$, $\Lambda_B^{444} = 2.25$ μm: a), c), e) – experiment; b), d), f) – simulation.
Fig. 3 $I_h(q_x, q_z)$, S3, t=70.71 μm, Cu $K_{\alpha 1}$. Experiment: a) (444), $\Lambda_B^{444} = 2.25$ μm, c) (888), $\Lambda_B^{888} = 12.82$ μm, e) (880) $\Lambda_B^{880} = 13.24$ μm. Simulation: b) (444), d) (888), f) (880).
Table 1 Growth parameters of $Y_{2.93}La_{0.07}Fe_5O_{12}$ epitaxial films. R_1=Fe_2O_3/Y_2O_3, R_3=PbO/B_2O_3, R_4=garnet/(garnet+solution), K_1=Y_2O_3/La_2O_3 are the mass ratios of solution components.
Table 2 Average lateral column sizes and densities of screw $\vec{b}_s = a[111]/2$ and edge $\vec{b}_e = a[\bar{1}10]$ dislocations